IOP Publishing Plasma Sources Science and Technology
Plasma Sources Sci. Technol. **30** (2021) 095009 (13pp) https://doi.org/10.1088/1361-6595/ac1ee0

Stable filamentary structures in atmospheric pressure microwave plasma torch

Miroslav Snirer*, Jozef Toman, Vít Kudrle and Ondřej Jašek

Department of Physical Electronics, Faculty of Science, Masaryk University, Kotlářská 267/2, CZ-61137 Brno, Czech Republic

E-mail: snirer@mail.muni.cz

Received 8 March 2021, revised 18 July 2021
Accepted for publication 18 August 2021
Published 15 September 2021

Abstract

This paper experimentally investigates the processes governing the single- and multi-filament regimes in an atmospheric pressure microwave (MW) torch operated in argon. Optical emission spectroscopy and spectral imaging are the principal diagnostics techniques which are employed. MW power is found to be the main parameter controlling the number of filaments. The single-filament regime exhibits many properties typical for surface wave discharges, e.g. a linear decrease in electron density along the axis or the existence of a central dip in the radial/lateral emission profiles. Simple geometric quantities, such as the length or thickness of the filament(s), vary almost linearly with the input MW power, and exhibit discontinuities at successive filament splitting events. These take place at similar values of filament maximum thickness, and may be due to skin-depth limited power transfer. The presence and chemistry of a low-emission intensity plasma shell surrounding the filament(s) is also investigated. The gas temperature is estimated from the OH band and complemented by Schlieren imaging, which revealed that a much larger cone of gas is being heated by filaments than is their diameter.

Keywords: microwave plasma, surface wave, self-organization, filamentation, laminar flow

(Some figures may appear in colour only in the online journal)

1. Introduction

Plasma sources operating at atmospheric pressure are preferred in many applications [1–3] owing to their easy manipulation, low maintenance, and reduced costs by avoiding the vacuum systems.

However, the transition from a low to atmospheric pressure often leads to new difficulties. An originally stable diffusive homogeneous plasma may exhibit substantially different characteristics under new conditions, e.g. instabilities, non-uniformities, etc [4–7]. Among these, a radial contraction [8], forming a relatively thin dense plasma channel (filament) is one of the most common change that may be encountered. A large proportion of atmospheric discharges actually exhibit filamentary characteristics at the macroscopic or microscopic scale, e.g. lightning [9], sparks [10], arcs [11], glow discharges [7], dielectric barrier discharges (DBD) [12, 13], radio-frequency DBD jets (also known as atmospheric pressure plasma jets-APPJ) [14, 15], etc. For each category, the processes responsible for the channel contraction may differ.

This paper focuses on microwave (MW) discharges, which tend to be filamentary at atmospheric pressure. Various radially contracted plasma appearances have been reported, e.g. a single fast rotating filament forming an apparent cone structure in a microwave plasma torch (MPT) [16], a short bright filament (called dart) in an axially injected torch (TIA) [17], or a single filament in a surfatron jet [18, 19].

The process of the radial contraction of MW discharges has been most often studied using noble gases (Ar [8, 20], Xe [21, 22], Kr, and Ne [23–25]) but recently, it has also been investigated using CO_2 [26]. A finite thermal conductivity of

* Author to whom any correspondence should be addressed.

the gas leads to inhomogeneous heating [27], which was considered to be one of the main mechanisms [20, 23]. Later, it was shown [8] (at least for MW surface-wave discharges (SWDs)) that it contributes to the contraction mainly by creating more molecular ions (e.g. Ar_2^+) owing to a positive density gradient of neutral atoms. The dissociative recombination of these molecular ions causes higher electron losses, promoting the plasma channel radial contraction.

Under certain conditions, this dense plasma channel can even split into multiple filaments in a process called multi-filamentation. This phenomenon is usually observed at sufficient power levels in rare gas plasmas sustained in large-volume reactors or in free space, where plasma was not space limited, e.g. in MW cavity plasma [28], large-diameter tubular SWDs (surfatron [29, 30], surfaguide [31]), microdischarges [32], or by focussed MW beams (Ar [33], air [34, 35]).

There is also an important role for the high-frequency excitation of the plasma. The skin effect, which influences the power transfer, has been proposed as another mechanism that limits the high-frequency plasma diameter [24, 36], and thus contributes to its radial contraction. As stated above, with sufficient power, a configuration of multiple thinner filaments may be naturally favoured over a single thick filament [4, 23]. By investigating this multi-filamentation process in a MW cavity, the authors in [28] showed that it is related to changes in electron density, electron temperature, and the effective collision frequency for momentum transfer. Another theoretical study [37] showed that an increase in the electron–neutral collision frequency with electron temperature is a required condition for the multi-filamentation in recombination-controlled discharges at elevated pressures.

While filament splitting can be generally chaotic, the multi-filamented atmospheric pressure SWDs in tubular reactors often exhibit quite neat, quasi-parallel filaments with the electric field of the surface wave (SW) oriented axially [38]. In that paper, it was reported that their mutual distance decreases as their number increases, and they tend to be stationary in still argon atmosphere. Their origin was attributed to the development of ionisation-overheating instability. A variation of their number was supposedly caused by the interference of electromagnetic fields scattered by the filaments, and an arrangement that achieves the maximum absorbed power was presented.

Atmospheric pressure MW plasmas found their applications in areas such as surface treatment [39, 40], plasma medicine [41], hydrogen production [42], CO_2 conversion [43, 44], nanomaterial synthesis (nanoparticles [45, 46], nanotubes [47, 48], and graphene [49, 50]). In many of these applications, a filamentary or multi-filamentary character is actually undesired, and different approaches have been devised to prevent it.

Plasma jets may confine the plasma inside a small-diameter dielectric tube to prevent the multi-filamentation by the dampening of small perturbations via a diffusion to the walls (radius limitation effect) [51]. It is also often used to facilitate spatial and temporal measurements on single-filament plasmas [52].

Another approach is to use an admixture to prevent radial contraction and multi-filamentation, as was shown in the study by Martinez *et al* [27]. Their pure rare gas (Ne) plasma exhibited radial contraction and multi-filamentation at atmospheric pressure. Small admixture ($\leqslant 1\%$) of another noble gas (Ar/Kr) with a lower ionisation potential inhibited both radial contraction and multi-filamentation, making the discharge homogeneous. The diffusion of admixture atomic ions caused the loss of charged particles in the plasma, interrupting the kinetics previously leading to dissociative recombination [23]. This resulted in plasma expansion and the disappearance of radial contraction and multi-filamentation.

The importance of the admixing of the surrounding gas was also shown by Xian *et al* [53], who investigated the influence of the working gas and surrounding gas on the filamentation and formation of plasma bullets in (APPJ). The discharge became radially contracted and multi-filamentary when the metastable states of the working gas (Ar, Kr) had lower energy than the ionisation potential of the shielding gas.

Altogether, there is a strong practical motivation (besides the obvious scientific curiosity) to study the filamented and multi-filamented plasmas, together with processes that can affect them, and the goal of this study is to gain an understanding and control of these processes.

Despite long and intensive research, the self-organisation in multi-filament patterns remains unclear. The presented paper tries to better explain this issue by providing experimental observations of the multi-filamentation process in a free expanding argon MW plasma torch. In contrast with many published works [16, 28, 29, 38, 53–55], we observed in a repeatable fashion a stable plasma structure that was formed by up to three filaments, i.e. it was not changing or moving in any way. It studies the influence of external parameters on the observed number of filaments and the general behaviour of the discharge. It is motivated by an often asked but seldom answered question: is the reason for the filament branching the length, temperature, width, power density, or something totally different? Consideration is also given to the experimental evidence to determine whether or not a SW is propagating along the filament(s).

2. Experimental set-up

Plasma filamentation is observed using a custom-built MPT using the schematic view presented in figure 1. This type of MW plasma source of coaxial geometry is similar to an axially injected torch (TIA) [56, 57] or a waveguide-based axially injected torch TIAGO [58]. However, its operational conditions are closer to those of the MW plasma torch described in [55]. MW power (10–300 W) is supplied by a 2.45 GHz Muegge magnetron generator. The MW line using a WR340 standard waveguide consists of a water-cooled ferrite circulator, a bi-directional −50 dB coupler to incident and reflected diode power metres, a three-stub tuner and a ridge waveguide transition to a perpendicular coaxial line.

The inner conductor of the coaxial line is hollow and allows the introduction of gases into the discharge chamber through an exchangeable graphite nozzle (length 18 mm, outer diameter 8 mm) with a 0.8 mm diameter axial orifice. The nozzle configuration is the same as in our previous papers [49, 59, 60],

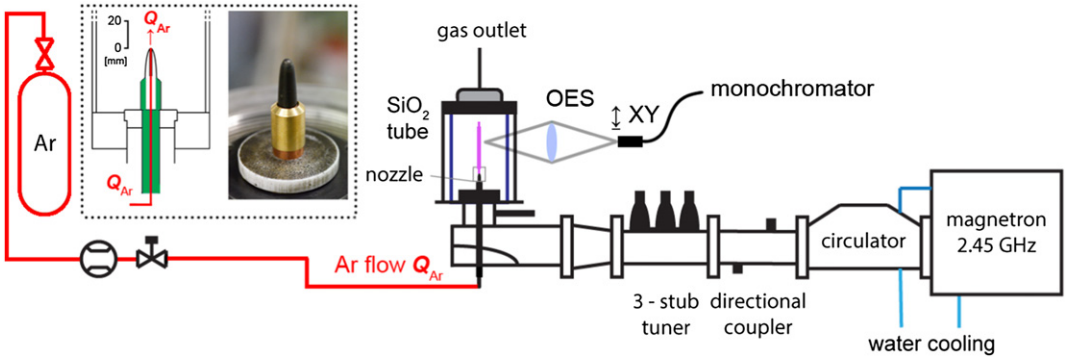

Figure 1. Schematic drawing of the experimental set-up. The photographic insert shows the graphite nozzle on top of the brass inner conductor. Its configuration is the same as in our previous papers [49, 59, 60], but its secondary gas channel (green in the schematics) is unused and sealed off.

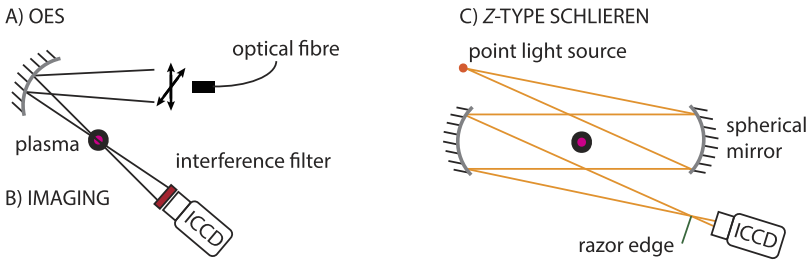

Figure 2. Schematic drawing of the diagnostic part of the experimental set-up: (A) OES, (B) spectral imaging and (C) Z-type Schlieren imaging.

but its secondary gas channel (green in the schematics) is unused and sealed off. Argon (99.999% manufacturer's specified purity) is used as a working gas, its flow rate being controlled by a Bronkhorst mass-flow controller with the typical values in the range $Q_{Ar} = 300–1200$ sccm.

The nozzle is placed vertically in a cylindrical fused silica discharge tube with a length of 200 mm and a diameter of 80 mm. The duraluminium bottom flange is o-ring sealed to the discharge tube and mated to the outer conductor of the dielectric-sealed coaxial line. The o-ring sealed duraluminium top flange is placed 120 mm from the nozzle, and it contains a central 40 mm exhaust port which transitions to a long polyethylene hose via a nipple. Both flanges are in contact with a grounded 150 mm diameter cylindrical protective mesh preventing MW leaks.

An overview OES is performed using Avantes ULS3648TEC (200–1000 nm) fixed grating (300 gr mm^{-1}) spectrometer with a spectral resolution of 1.4 nm. The higher resolution needed for the temperature calculation is provided by a Jobin Yvon Triax 550 spectrometer (3600 gr mm^{-1} diffraction grating) equipped with liquid nitrogen cooled CCD. The optical system for OES uses an ultraviolet-visible (UV–VIS) coated spherical ($f = 20$ cm) mirror to magnify the plasma filament for spatially resolved measurements, as can be seen in figure 2(A). The optical fibre is placed in a projection plane, and is mounted on a manually adjustable linear XY translation stage.

Imaging of the plasma filaments (see figure 2(B)) for geometry analysis is carried out using a Princeton Instruments PI-MAX 3 ICCD camera equipped with a Sigma 105 mm macro lens. Spectral imaging is performed through a set of interference filters (250 nm for NO, 310 nm for OH, 355 nm for CN, and 826 nm for Ar). Nikon D5200 DSLR equipped with a 50–200 mm Nikkor lens records high-resolution colour images ($f/10$, ISO 500, 1/500 s). Matlab with the Image Processing Toolbox and DipImage/DipLib library [61] was used for image processing and analysis. The inverse Abel transformation of the lateral profiles into the radial profiles was performed by using the PyAbel library [62].

Schlieren imaging (see figure 2(C)) can visualise the gas flow and uses a Z-type configuration of two aluminised first-surface spherical mirrors (1.5 m focal length, 150 mm diameter, $\lambda/8$ surface precision), razor edge, high-power white Luminus LED (CFT-90-WDS-X11-UA500) and ICCD camera (Princeton Instruments PI-MAX 3 with Sigma 105 mm macro lens).

3. Structure of plasma produced by MW torches

Axially injected MW torches (e.g. MPT, TIA, TIAGO) operating at atmospheric pressure are usually fed by a waveguide, which enables a higher MW power compared with a flexible coaxial cable feed, and so an integral transition from TE_{10} waveguide mode to rigid coaxial TEM mode is often included [63]. Plasma is excited at the tip of the central coaxial electrode or inside its axial gas channel; the gas flow then expands it freely into the surrounding atmosphere.

According to [64], plasma produced in our experiment should be similar to surfatron or surfaguide [65] discharges, sustained by a SW propagating along the dense plasma

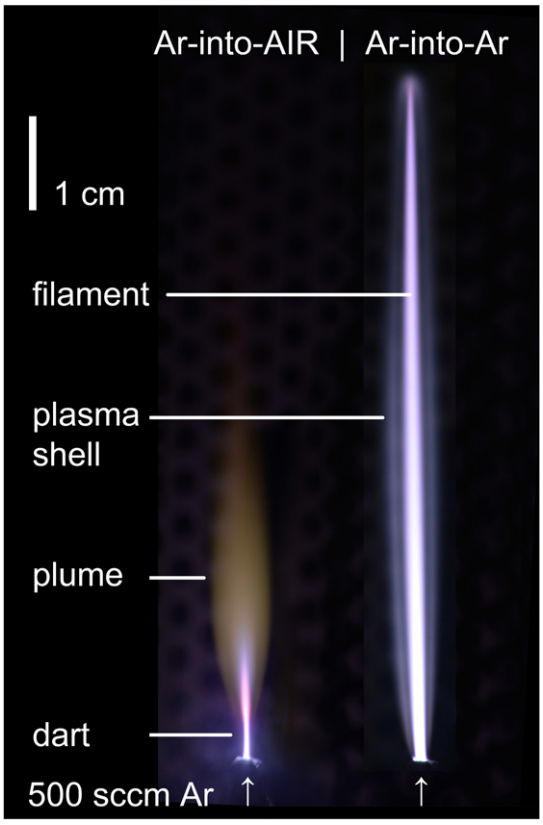

Figure 3. Illustrative photograph of the MPT argon plasma freely expanding into air (left) and argon (right) atmospheres—P_{MW} = 50 W, Q_{Ar} = 500 sccm.

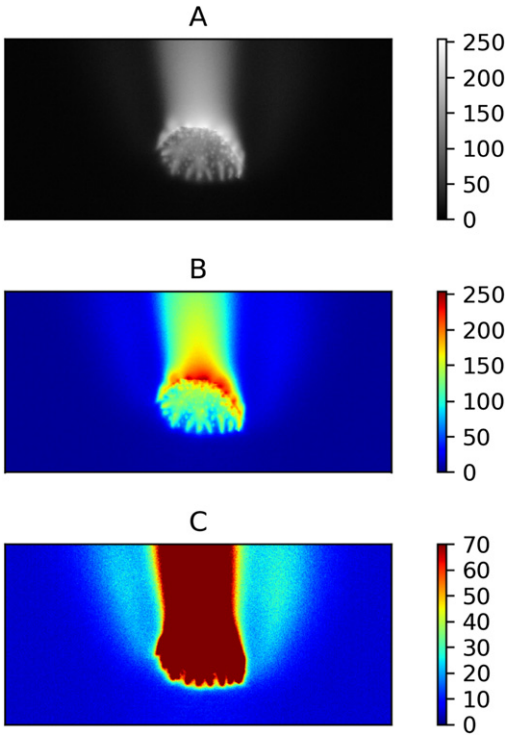

Figure 4. Electrode spot on the graphite electrode, (A) greyscale photograph, (B) same photograph in false colours, (C) different colour-scale enhancing the visibility of plasma shell around the filament proper—P_{MW} = 50 W, Q_{Ar} = 500 sccm. The width of the image(s) corresponds to 16 mm.

filament (except the dart region), as it was theoretically proposed previously in [66]. The non-ionised gas forms a virtual cylinder around the plasma, creating an interface for the wave propagation due to a change in relative permittivity.

Owing to its ease of operation, the noble gas is often used in MPTs as a working gas (e.g. He in [63] or Ar in [16, 17]). Expanding into the surrounding atmosphere may significantly impact the plasma [67]. In the case of air as an ambient atmosphere, it leads to the formation of a flame-like plasma structure, as can be seen in figure 3(left). Plasma consists of two distinct luminous regions: an initial 'dart', which is a short, bright, narrow channel (10–15 mm length, 1 mm diameter) surrounded by a low-intensity plasma shell, and which transitions to a later stage 'plasma plume', which is wider and less intense, and where the vigorous gas mixing occurs [17, 57, 64].

In a plasma jet expanding into a noble gas atmosphere, the electron energy is not lost in the dissociation and excitation of air molecular species. The recombination region of the plasma plume diminishes, and the filament in the dart region grows into one or (if MW power is sufficient) multiple long bright filaments. These are usually very turbulent and the plasma becomes highly unstable, complicating further studies [16]. Oscillations are usually caused by the movement of the electrode emission spots or by arcing inside the electrode gas channel. Increased nozzle erosion and random changes in MW absorption prevent optimal tuning/matching and hinder the long-term stable operation of the experimental set-up. Some aspects of axial torches are therefore more difficult to study in pure Ar than in Ar with admixtures or free expanding into air.

Interestingly, in some cases, the fast movement of filament(s) can lead to the formation of a macroscopically stable structure. A single gyrating filament creating an apparent cone structure was observed and studied in argon MPT [16, 55].

We found that it is possible to achieve a stable filament in a rather pure Ar atmosphere (see figure 3(right)) by using a graphite electrode. In this case, the electrode spot is formed on the outer surface of the nozzle, which is in contrast with metallic (stainless steel, copper) electrodes, where the filament originates inside the central gas channel. The electrode spot on the graphite electrode covers an area which is considerably larger than a cross-section of the filament, see figures 4(A) and (B). The macroscopically diffuse spot actually consists of many tiny microspots, each with its own submillimeter microfilament. These microfilaments diffusively join to form the base of the macroscopic filament. While both the macroscopic electrode spot and the filament remain rather stable, the microspots and attached microfilaments move, appear, and disappear. Currently, without further detailed investigation, it is difficult to determine whether the different behaviour of metallic and graphite electrodes stems from different electrical conductivity, thermal conductivity, work function, or other cause(s).

The graphite electrode was rather resistant to erosion. During a single experimental run, no changes were observed, but

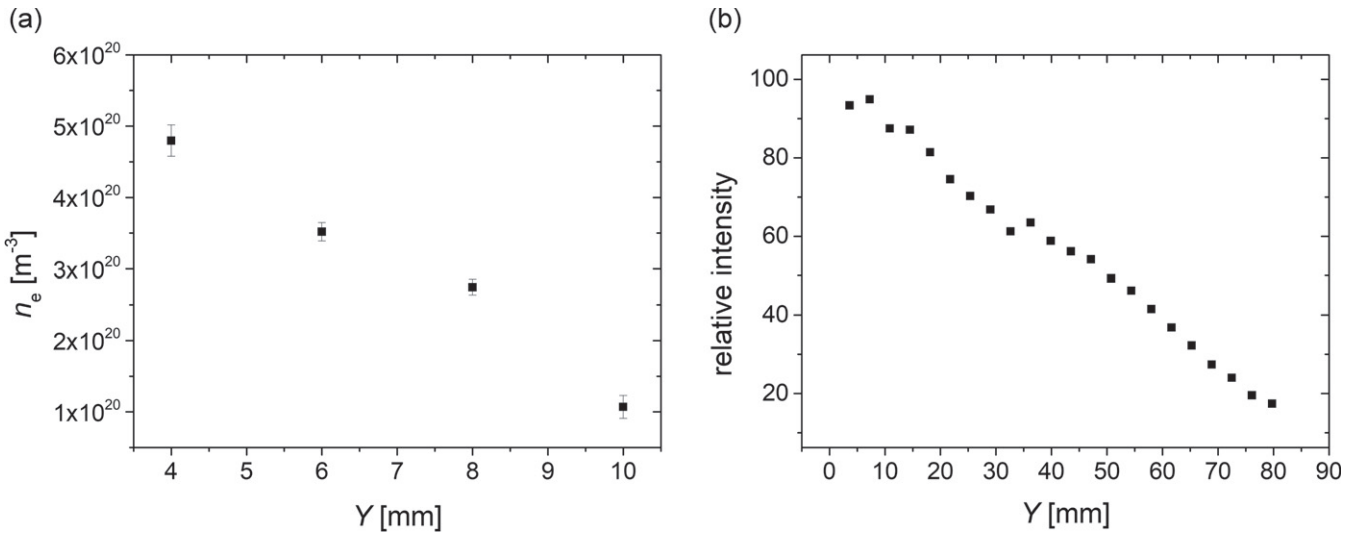

Figure 5. (a) Axial profile of the electron density calculated from the Stark broadening of H_β (45 W, 1000 sccm Ar, 10 sccm H_2) and (b) the axial argon (419 nm, OES) emission intensity profile (50 W, 500 sccm Ar) in the single-filament regime.

after many tens of hours of operation, there was some rounding of the edges, etc. However, such small variations in the shape of the graphite electrode had a negligible influence on the plasma.

The gas flow used in this study (500 sccm corresponds to average axial velocity 16 m s^{-1}) ensures subsonic and non-turbulent flow conditions (Reynolds number Re < 2000, Mach number Ma < 0.3), which in turn promotes the formation of a stable laminar filament(s).

4. Results and discussions

4.1. Single-filament regime

It was found that the MW power was the main parameter that controls the plasma properties. For values below approximately 60 W, the discharge has the form of a single stable filament, enabling detailed diagnostics.

In many aspects, the single-filament regime exhibits many similarities with surface-wave driven atmospheric pressure plasmas, such as surfatron or surfaguide [64]. Generally, the electron density axial profile should decrease nearly linearly from a maximum near the launcher towards the minimum at the end of the filament, where it descends below a critical value, preventing the further propagation of the SW. The input MW power should directly affect the maximum n_e value, and consequently, also the plasma length. Figure 5(a) shows an axial profile of n_e calculated from the measured H_β Stark broadening (following the procedure described in our previous papers [59, 68]) after admixing a small amount of hydrogen to the working gas. However, the hydrogen admixture affects the plasma, so the experimental conditions are slightly different from those typically used in this paper. Nevertheless, the expected linear decrease of n_e is evident.

Actually, the more precise theory and experiments in [64] indicate that the initial plasma segment closest to the wave launcher (in our case the nozzle) should be sustained by non-guided (space-wave) [64] radiation, and so this section usually has a higher electron density and higher emission intensity, and it locally departs from the linearly decreasing predictions discussed above. Although the data in figure 5(a) are not sufficiently detailed to show this behaviour, it was confirmed by the previous measurements on our device [68, 69].

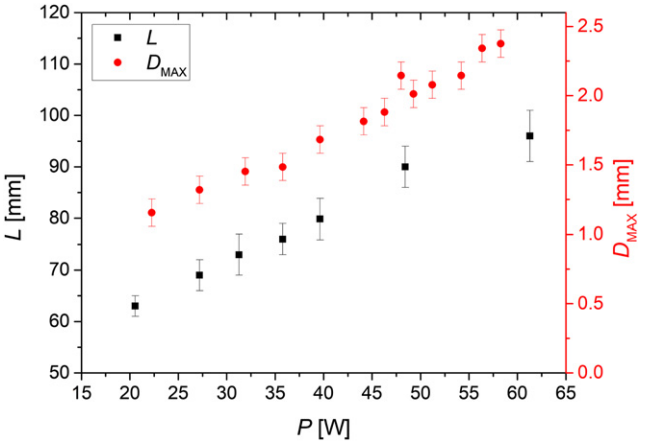

Figure 6. Dependence of single-filament length and maximum diameter on the MW power (up to a filament splitting threshold) for 500 sccm Ar.

The linear decrease of the relative emission intensity along the filament shown in figure 5(b) also has characteristics typical of SWD.

As explained in [65], the length of SW plasma should be a linear function of the supplied power. Up to a filament splitting point, we observed a linear dependence of the length on P_{MW} (see figure 6).

The thickness of the filament at any position Y can be quickly determined from image analysis, setting an intensity threshold e.g. at 80%. As the thickness is not constant along the filament length (typically, it has a local maximum in its first third), we have chosen the maximum diameter as a

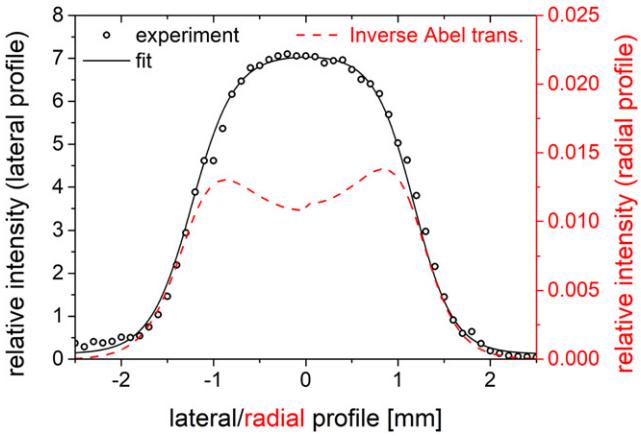

Figure 7. Lateral/radial emission intensity profile (Ar 921 nm) derived from OES—$Y = 40$ mm, 50 W, 500 sccm Ar.

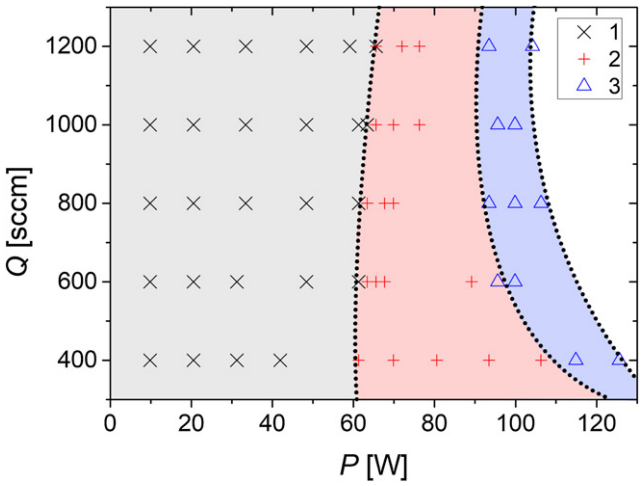

Figure 8. Operating diagram, i.e. map showing the variation of the number of filaments with the operating conditions: delivered MW power P_{MW} and argon flow Q_{Ar}.

suitable geometric parameter and plotted it in figure 6 as a function of MW power. The figure shows that the maximum diameter of the filament grows linearly with increasing MW power.

Figure 7 shows the measured lateral emission intensity profile together with the corresponding radial profile (calculated using the inverse Abel transformation). The radial profile exhibits a local minimum in the centre of the filament. This is again in agreement with a typical hollow structure (so-called M-profile) of SWDs [63, 64, 67], which is caused by the MW electric field being strongest near the filament surface (skin effect) and the weakest near the axis. The collisional skin depth can be calculated as [70]:

$$\delta = \frac{\sqrt{2}c}{\omega_{pe}}\sqrt{\frac{\nu}{\omega}}, \qquad (1)$$

where c is the speed of light in vacuum, ω_{pe} is the electron plasma frequency (rad s^{-1}), ν is the collision frequency for momentum transfer (s^{-1}), and ω is the MW angular frequency (rad s^{-1}). The equation is valid if $\omega_{pe}, \nu \gg \omega$. Depending on

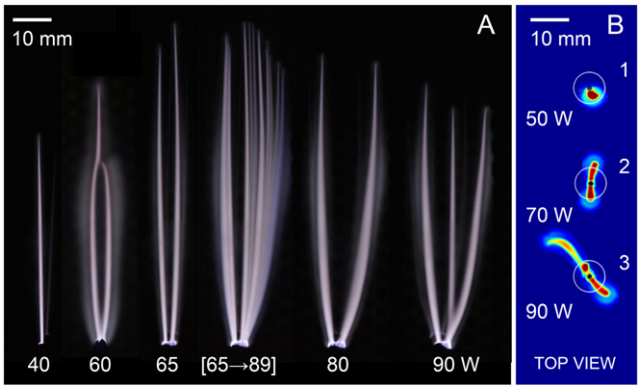

Figure 9. Illustrative photographs of multi-filamentation depending on input MW power, with a constant argon flow rate $Q_{Ar} = 500$ sccm: (A) side view, (B) top view with pseudo coloured intensity. Side view images in the 65–89 W power range are overlapped to show the gradual movement of the second filament.

the electron density (1–5 $\times$ 10^{20} m^{-3}, see figure 5(a)) and collision frequency (10^{10}–10^{11} s^{-1} [68]), the calculated skin depth values (in 0.3–1.9 mm range) are close to the observed filament radii (see figure 6). The radial profile in figure 7 indicates a sub-millimetre skin depth.

4.2. Multi-filament regime

By varying the external parameters—MW power P_{MW} and gas flow Q_{Ar}—over a wide range, the operating diagram in figure 8 was constructed. By increasing P_{MW}, the number of filaments increases, forming up to four filaments. While a configuration with one or two filaments is very stable and somewhat independent of Q_{Ar}, additional filaments lead to the destabilization of the system (compare the areas of 1, 2 and 3 filament regimes in the operational diagram). In such a case, a very small change in P_{MW}, Q_{Ar} or a slight random movement of the electrode spot may cause a disintegration of the stable filament structure, often forming an unstable bunch of arc-like plasma channels with one end on the inner coaxial electrode and the second end on the dielectric wall of the discharge tube or on the exposed metallic wall of the outer coaxial conductor [71]. This made it somewhat difficult to study any regime with more than two filaments. Actually, the four-filament regime is so sensitive that it was observed only once, and this observation could not be repeated. Therefore, in the following text and figures, a maximum of three filaments are discussed in detail.

The operating diagram confirms that P_{MW} is truly the primary control parameter, influencing the plasma properties and the number of filaments. The parameter space was also tested outside the depicted zone. Gas flows over ≈1300 sccm induced turbulence and/or oscillations caused by electrode spot movement. With an argon flow rate under ≈300 sccm, there was too much contamination by air impurities, preventing a multi-filamentation regime. For MW power higher than ≈120 W, there was no stable configuration of filaments.

Illustrative photographs documenting progressive multi-filamentation are shown in figure 9(A). To complement this side view, the plasma was also imaged from above through

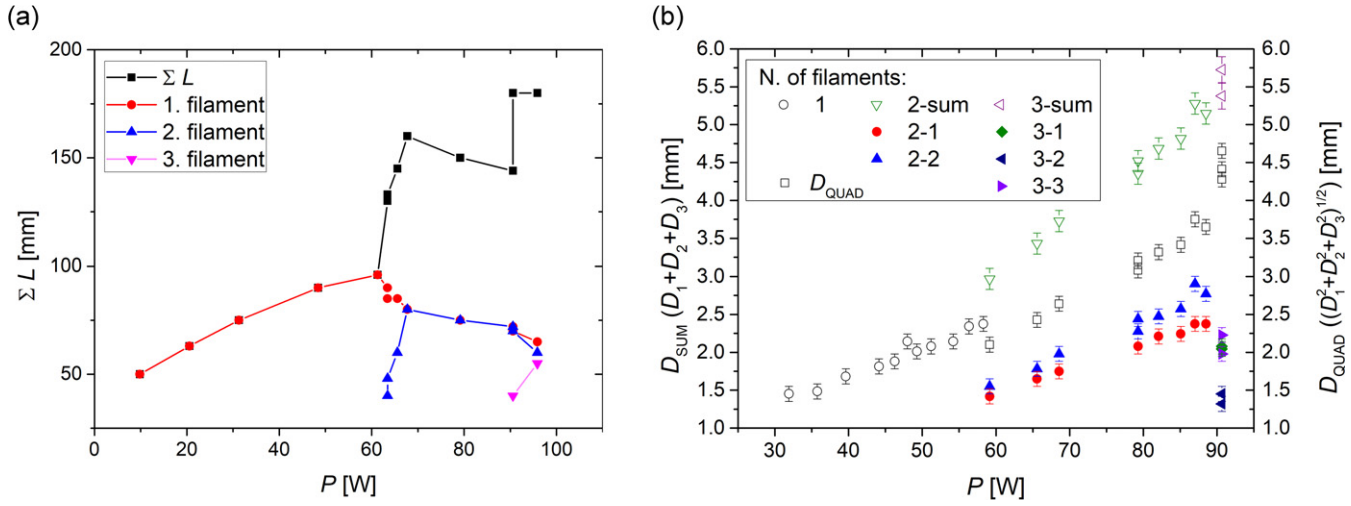

Figure 10. Dependence of the geometric quantities on P_{MW} for 500 sccm Ar: (a) filament length(s) L and their summed values $\sum L$, (b) maximal values of diameters $D_{1,2,3}$, their D_{SUM}, and quadratic diameter D_{QUAD}.

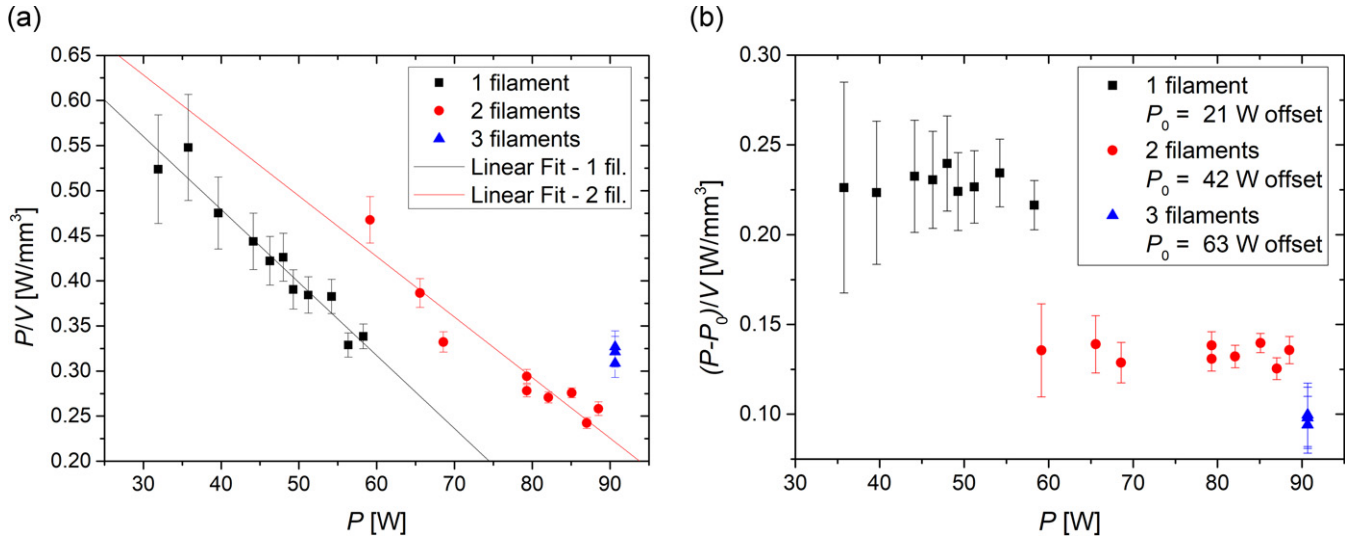

Figure 11. Dependence of the power density in filaments on input MW power P_{MW} for 500 sccm Ar: (a) power density P/V and (b) corrected power density $(P\text{-}P_0)/V$ for radiation losses by subtracting a specific offset P_0.

a window in the upper flange, resulting in the images in figure 9(B) (pseudo coloured for better visibility). The white circle denotes the position and size of the nozzle (outer diameter 8 mm), while the small black spot is the central gas channel. A single filament (top subfigure) sits above its electrode attachment point, which is on the outer side of the conical nozzle close to the circular edge of the central gas channel. Although the position of the filament on the nozzle is not exactly axial, its relative intensity map is quite circular.

After a new filament is formed at 60 W, there is a small range of P_{MW} up to 65 W, where the second filament increases in length until it matches the first one (2nd and 3rd sub-image). Subsequent movement due to changes in P_{MW} can be better visualised by overlapping a sequence of images (fourth sub-image of figure 9(A)). A closer look at the overlaid image reveals that one (parental) filament stays in its position, while the other moves laterally away, linearly increasing the distance between them.

The middle sub-image in figure 9(B) shows the situation of two filaments from the top view. Markedly asymmetric plasma shells are present near both filaments. They are substantially stronger on the outer side (wall facing) of the filaments. The top view images prove the existence of plasma shells, which may be mistaken as mere wall reflections or artefacts in figure 9(A).

At $P_{MW} \approx 90$ W, the 'moving' filament splits again, forming a third one between them. While each of the two original filaments has its own electrode attachment point, the new one is fainter, narrower, and has a common base with its parental filament. The top view of this situation is shown in the lowest sub-image of figure 9(B). It should be noted that these three filaments are not positioned in an intuitively expected radial

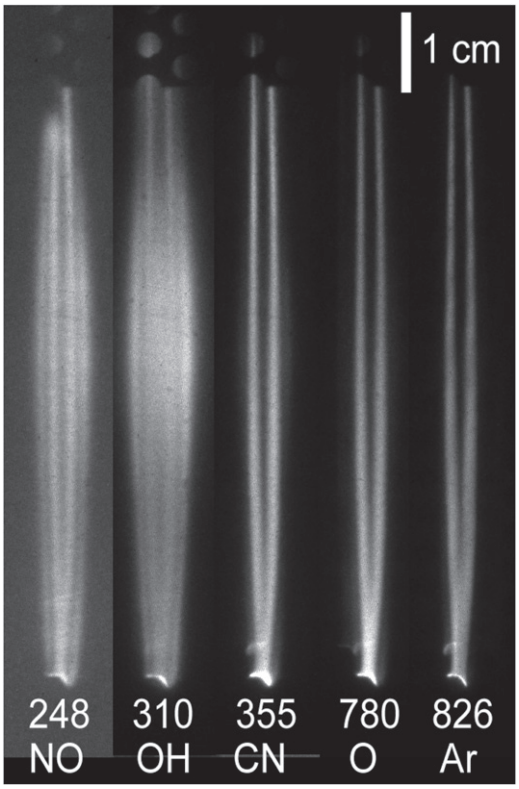

Figure 12. Set of images of two filaments taken by ICCD through spectral filters (indicated by central wavelength in nm and the corresponding species). Experimental conditions were 70 W, 500 sccm Ar.

symmetry (i.e. forming an equilateral triangle), but in a planar configuration. This is not an isolated incident, but a typical outcome. This is in direct contradiction with theoretical studies [37, 72, 73] which predict a radial symmetry for multi-filament patterns. A speculative explanation could be that multiple filaments are not equivalent, and consequently, the 'repulsion' between them is not the same.

The three-filament configuration is very sensitive to any fluctuation in the experimental condition, and its plane of symmetry tends to rotate slowly. This indicates that the planar pattern observed is not caused by some nozzle or reactor irregularity. Twisting or rotating filament structures are actually not unknown, as previously reported, e.g. in [29, 54].

Unfortunately, it was not possible to determine n_e in a multiple-filament regime, as the hydrogen admixture that is required for H_β Stark broadening had a significantly negative impact on multi-filamentation.

The influence of MW power on filament length, as presented in section 4.1 for a single-filament case only, also occurs for multiple filaments, see figure 10(a). After a splitting point near 60 W, the new filament (blue curve) grows rapidly, while the parent filament (red curve) shortens slightly. At around $P_{MW} \approx 65$ W, their lengths become equal. It is interesting to note that between 66 W and 90 W, the lengths of both filaments actually decrease with increasing P_{MW}. If the MW power increases further, at ≈90 W, there is another splitting, which results in three filaments. Again, the new filament (pink curve) grows rapidly, while the two other filaments decrease in length. The black curve in the same figure represents the sum of all filament lengths. It exhibits non-monotonous characteristics and sudden jumps at splitting points, and confirms the nonintuitive behaviour of the filaments' length in the 65–90 W range.

Figure 10(b) shows the influence of the MW power on the maximum diameter of the filament(s). In section 4.1, it was already established that in the single-filament regime, the maximum diameter depended linearly on the MW power. Then, at the first splitting point ($P_{MW} \approx 60$ W), there appear two filaments (designed 2–1 (original, nearly unmoving one) and 2–2 (laterally moving one)) instead of one. Their diameters also vary linearly with the MW power, while the new filament is always thicker than the original. At the second splitting point ($P_{MW} \approx 90$ W), this thicker filament splits again, so there are now three filaments, designed 3–1, 3–2, and 3–3. Even higher MW powers are difficult to study because of the low stability of the three-filament configuration (see discussion concerning figure 8 above). The splitting to four filaments happens around 110 W, but this value cannot be considered as reliable.

It appears that the splitting off a new filament occurs at a certain critical value of the parent filament diameter—both transitions from one to two filaments and from two to three filaments occur at a diameter of around 2.5–3 mm. This is also supported by the careful examination of the second subimage from the left (60 W) in figure 9(A), where the splitting occurs at the widest part of the filament. A similar splitting of one filament was observed by [24] in tubular reactors with a surfaguide launcher, where the single filament increased in diameter as the power per unit length increased, breaking up into more filaments at higher power. This could be caused by limited power transfer owing to the skin effect, as was discussed in section 4.1. The filament radius at the splitting point falls within the calculated skin depth range (0.3–1.9 mm).

In the same figure, the sum of all particular maximum diameters is plotted using hollow data points. It is interesting to note that this curve (in contrast to the summary length in figure 10) is monotonic, rather smooth (with only a minor jump near the 60 W), and even appears to be piecewise linear. Even better is the quadratic diameter ($D_{quad} = \sqrt{D_1^2 + D_2^2 + D_3^2}$), which should scale with the relative cross-sectional area. This supports the hypothesis that the diameter (and not the length for example) is the critical parameter for filament splitting, which was reported in the study [28].

Another interesting parameter is the power density. We calculated the total volume V of the filaments and plotted the power density P/V as a function of the input MW power P_{MW} in figure 11(a). As can be seen, it is not constant, but decreases with P_{MW}, and there are jumps after the splitting of the filaments. This may be caused by the power loss resulting from space wave radiation before the establishing of SW. If we incorporate an offset $P_0 \approx 21$ W it is possible to obtain almost constant power densities $(P - P_0)/V$ for the single-filament configuration, as can be seen in figure 11(b). To obtain a constant characteristic for the two-filament configuration, it is necessary to double this value, arriving at $P_0 \approx 42$ W. There

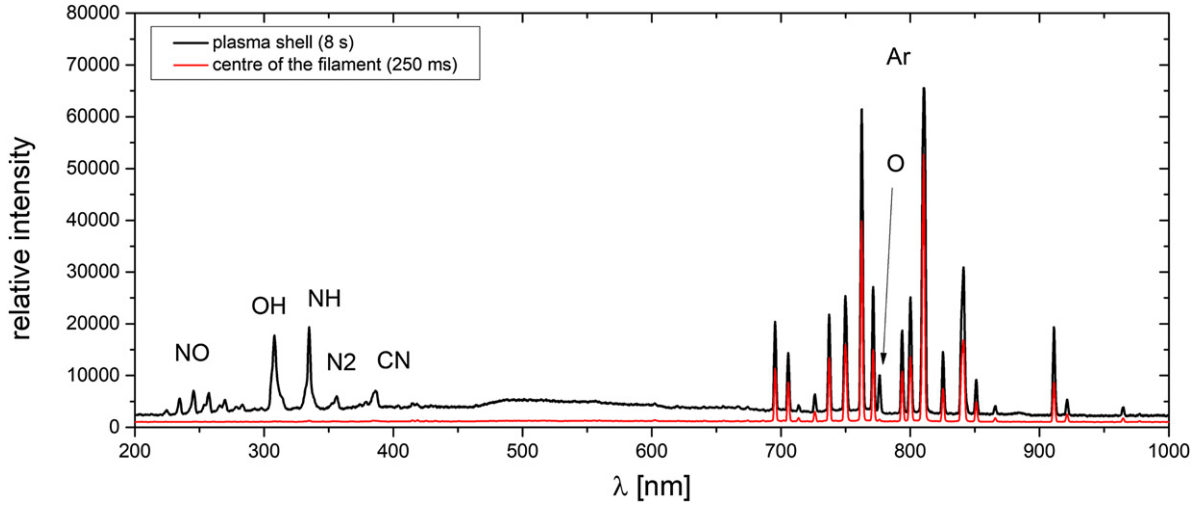

Figure 13. Overview emission spectra of the filament centre (integration time 0.25 s) and of the plasma shell (integration time 8 s). Experimental conditions were $Y = 40$ mm, $P_{MW} = 50$ W, $Q_{Ar} = 500$ sccm.

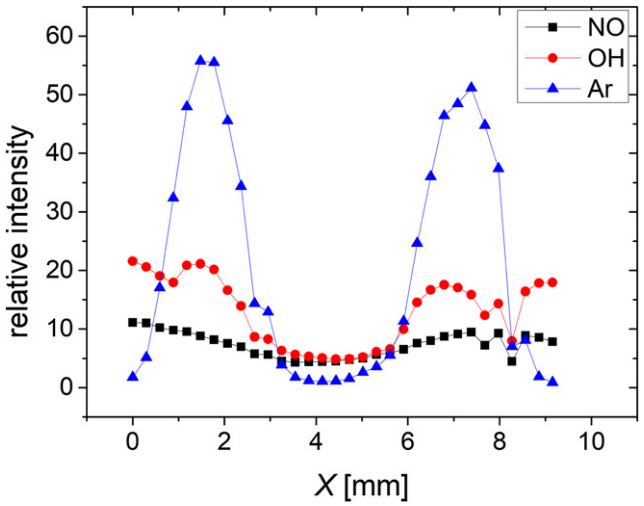

Figure 14. Lateral emission profiles of OH, NO and Ar for two filaments as derived from OES. Experimental conditions were $P_{MW} = 75$ W, $Q_{Ar} = 500$ sccm, $Y = 40$ mm.

is only one value for three filaments, so this quite interesting trend could not be verified further.

As discussed above, there are several strong hints that the filament carries the SW wave, which in turn excites it. While such a mechanism of SW propagation along a single filament appears to be nonproblematic, it becomes more complicated in the multi-filament regime. It is still an unresolved issue with respect to determining whether the SW propagation along the filaments is individual (many independent waves, each on its own filament) or collective (essentially, a single wave sharing power with each filament). Several studies reported that the maximum electromagnetic field intensity is at the interface between plasma and the surrounding medium (MPT [64, 66, 69], TIA [74]). SWDs should have a quasi-exponential decline (principally similar to evanescent waves) of electromagnetic field intensity away from the filament's surface, but a $1/r$ decrease was found for MPT [64, 69].

Actually, the model in [69] predicted that besides the main absorption maximum inside the filament, there should be a second smaller maximum of absorbed power density just radially outside of the filament proper. This could correspond to the plasma shell—a low-intensity glow around the filament, which is observable in figures 3, 4 and 9. In the single-filament regime, the plasma shell has a cylindrical shape surrounding the whole filament, while in the case of two filaments, the plasma shell is observable mainly at their outer sides, i.e. closer to the wall. The third filament usually has the plasma shell only at one side, facing the same direction as the shell of its parental filament. These asymmetries were not considered in [69], but it predicted that near the axial end of the plasma filament, there should also be a heightened power absorption [18], exhibiting a more intense 'cap' sitting at the filament tip. This cap should also be the place at which the plasma shell finally meets the plasma filament. This can be precisely observed in figure 3(right).

Using OES and spectral imaging (see figure 12 and figure 13), we found that emissions of the plasma shell consist mainly of molecular bands of NO–γ ($A^2\Sigma$–$X^2\Sigma$) and OH ($A^2\Sigma^+$–$X^2\Sigma$), i.e. the impurities. The experimental set-up is reasonably air-tight and flushed with argon, but small traces of air and humidity persist. It should be noted that a presence (even significant) of molecular bands in a rare gas emission spectrum cannot be directly interpreted as a proof of gross contamination. For example, Bogaczyk *et al* [75] reported the emission of an N_2 (1st negative system (FNS), 2nd positive system (SPS)), NO–γ, and OH in pure helium with less than 10 ppm of nitrogen (which is arguably a rather pure environment) resulting from high concentrations of helium metastables and Penning ionisation. In our case, it appears that below a certain threshold concentration (which is higher than the amount of impurities we routinely achieve in the apparatus) the impurities do not significantly affect the single-filament geometrical properties or the multi-filamentation process. The presence of impurities could be considered 'fortunate', as they

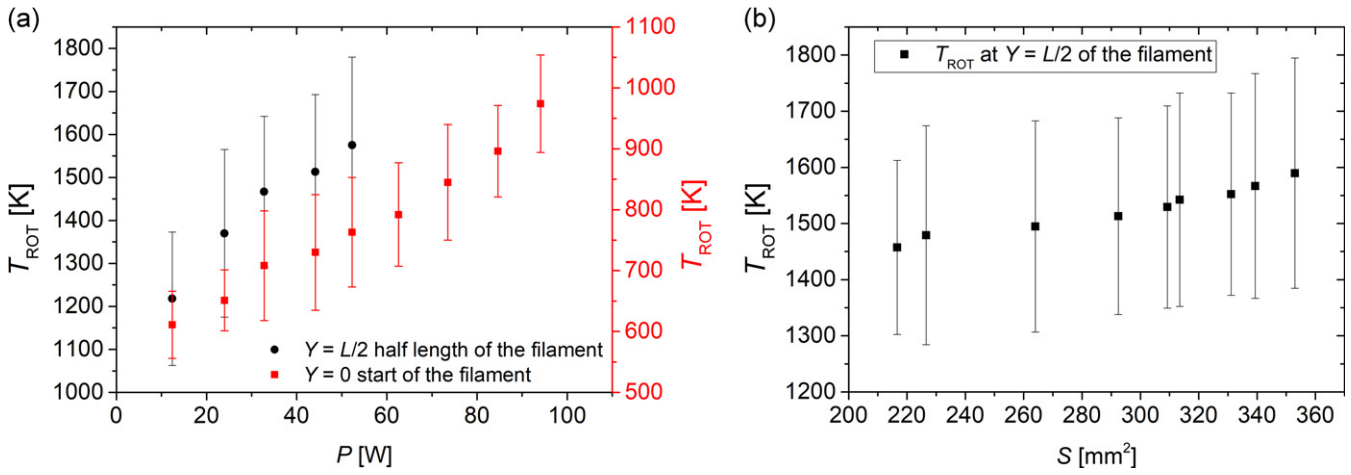

Figure 15. Gas temperature estimated from OH(A–X) rotational distribution—$Q_{Ar} = 500$ sccm: (a) power dependence of temperature measured at the start (near the electrode) and in the middle of the filament, (b) temperature measured at half the length of the filament as a function of its total surface area (corresponding power range is 30-60 W).

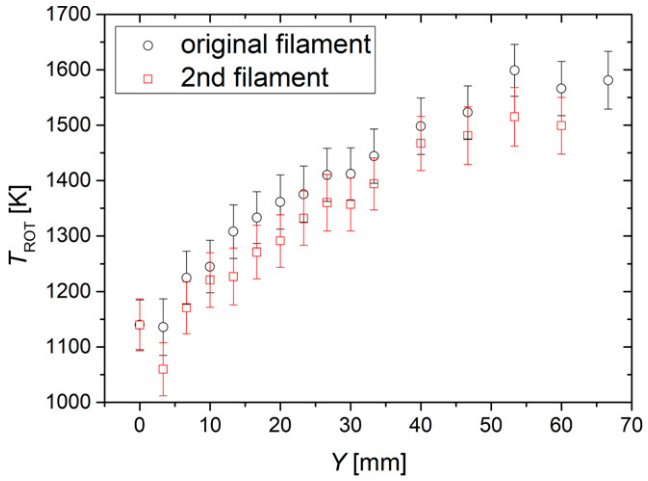

Figure 16. Axial profile of OH temperature along both filaments of a two-filament configuration. Experimental conditions were $Q_{Ar} = 500$ sccm, $P_{MW} = 65$ W.

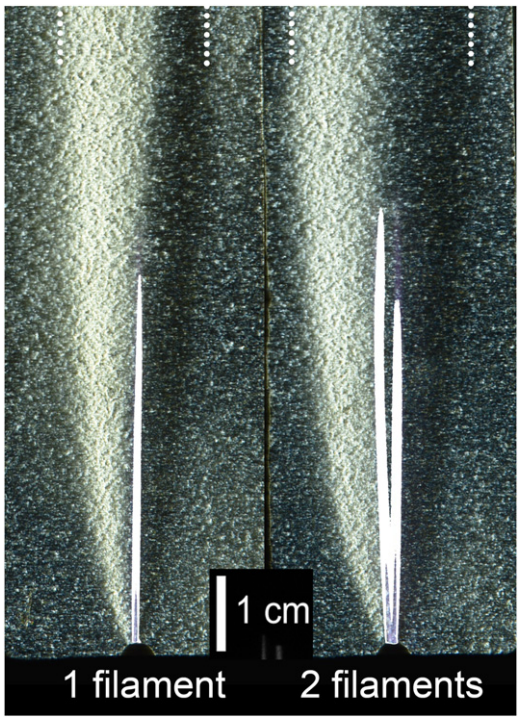

Figure 17. Schlieren images of one- and two-filament configurations, visualizing the expanding cone of hot gas −40 W and 70 W, 500 sccm Ar.

make the plasma shell discussed in the previous paragraph visible (owing to their lower excitation energy).

These impurities may be excited by different mechanisms, such as direct electron impact excitation, Penning excitation/ionization by energetic Ar species (e.g. Ar^*(11.56 eV), Ar^+(15.8 eV), argon metastables (11.55 eV, 11.72 eV)), or a specific mechanism such as Zeldovich for NO: ($N_2 + O \leftrightarrow NO + N, O_2 + N \leftrightarrow NO + O, N + OH \leftrightarrow NO + H$). However, while the Zeldovich mechanism is usually considered for its origin [76, 77], a computational study [78] of Ar plasma source reported that the primary production of NO was from atomic oxygen and the first metastable state of nitrogen $N_2(A)$. However, this requires high densities of O and $N_2(A)$ [79]. Reactions leading to the loss of NO (into NO_2, N_2) have a higher reaction rate at lower temperatures, leading to lower concentrations of NO outside the filaments [78].

Excited OH states can be produced [80] directly by the dissociation process $H_2O\left(X^1A_1\right) + e \rightarrow H_2O\left(B^1A_1\right) + e \xrightarrow{dis.} OH\left(A^2\Sigma\right) + H + e$ (energy threshold approx. 10 eV) or by excitation from the OH ground state $OH\left(X^2\Pi\right) + e \rightarrow OH\left(A^2\right) + e$ (energy threshold approx. 4 eV).

The emission profiles for OH, NO, and Ar in figure 14 are not identical. This could be expected as their excited states have different origins, excitation energies, ground-state densities, spontaneous emission rates, etc. Similar discrepancies in the radial profiles of emitting species (He(I), N(I), O(I), H(I), N_2^+) were reported for the MW torch in He [63]. Intensities of both molecular species grow on the outer filament borders,

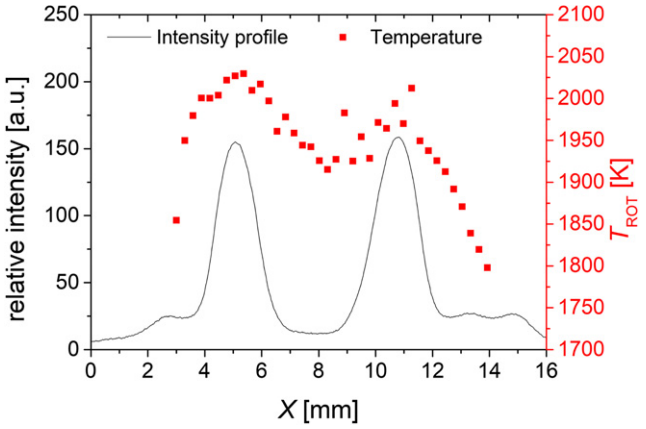

Figure 18. The gas temperature profile (red data-points) of two filaments—$P_{MW} = 75$ W, $Q_{Ar} = 500$ sccm, $Y = 40$ mm. For position reference, a lateral emission profile (black line) derived from ICCD imaging is also plotted.

which is consistent with the formation of the low-intensity plasma shell.

The rovibrational band of OH molecule is used to determine the rotational temperature T_{rot} by comparing measured OES spectra with the simulated ones obtained using the MassiveOES [81, 82] software. MW plasma torches operating at atmospheric pressure generally have an equilibrium between the rovibrational distribution of OH and the translational distribution of Ar gas, i.e. one can assume that $T_{rot} = T_{gas}$ [23]. Some authors [17] prefer to utilize N_2^+ because of the possible non-Boltzmannian distribution of OH upper states [82, 83]. Nevertheless, we have not found any such deviation in the OH Boltzmann plots, so we assume that using OH as thermometric species is valid. Many other groups [84–86] have also made the same assumption.

In this way, the rotational temperature at the filament start (near the electrode) is estimated and plotted in figure 15(a) (red data-points). The temperature at the middle of the filament (i.e. half-length) is also plotted in the same graph. Because the length is not a well-suited parameter (see the discussion of figure 10 above), the black data points are not plotted beyond the filament splitting point (≈60 W). Gas heating by MW power is mainly indirect via electrons [63, 87]. Nevertheless, both curves are nearly linear, and this trend continues even after the splitting of the filament(s). As the power increases, the filament should be heated more. However, as its surface area increases, the heat losses should also increase. A knowledge of the diameters at each position of the filament(s) from the imaging makes it possible to estimate their total surface area (approximation of circular cross section) and to plot it versus temperature, as in figure 15(b). It appears that these two processes are nearly equal. Doubling the power makes the temperature at $L/2$ increase by only 10%.

The axial profile of the OH rotational temperature is shown in figure 16 for the case of two filaments. The temperature is lowest near the nozzle and grows somewhat linearly with the position until it reaches the maximum at the filament(s) end. This is in agreement with the model of Ar MPT (500 sccm Ar, 250 W), which was reported by Synek *et al* [69]. The model showed that the heat conduction is the dominant energy loss channel in the region near the nozzle tip. The absorbed power density exhibited two maxima in the axial direction: first at the tip of the nozzle and second close to the end of the filament, where the gas temperature reached its maximal value. A gradual heating of the filament could also be caused by the limited cooling owing to reduced radial heat transport as the surrounding gas heats up. There is also a constant source of heating along the filaments by propagating SW, heating them steadily over their whole length.

Schlieren images in figure 17 show that a much larger volume of gas is heated, and not only the filaments themselves. The diameter of the expanding cone of hot gas is much larger than the maximal distance between two filaments. The cone diameter increases with the supplied MW power, as indicated by the dotted line segments in the upper part of the figure. The existence of this hot cone of gas explains why the filament temperature steadily grows even after filament splitting—the volumes of individual filaments are negligible compared to the whole volume of gas that is heated.

The low signal-to-noise ratio of Schlieren images (due to inhomogenities in the fused silica tube walls) hid any shape of the temperature profile between the filaments. To overcome this, the lateral emission and OH rotational temperature profiles were measured at larger filament separation values ($P_{MW} \approx 75$ W), see figure 18. The temperature profile exhibits a discernible dip of approximately 100 K between the filaments, which is nevertheless below a typical temperature calculation uncertainty of 200 K (10%). This also explains why it was not visible on the Schlieren image (figure 17). The rotational temperature falls steeply outside of the plasma, i.e. the filaments and plasma shell.

While the current study provides insight into the structure of the plasma and the process of filamentation, it is still limited to experimental observations. A purely theoretical approach inevitably requires many assumptions and simplifications, and can easily fail for overly complex systems, where chaos tends to reign. The authors believe that a numerical model that fully encompasses plasma physics, fluid dynamics, thermodynamics, electromagnetism, and inequilibrium chemical kinetics is important to fully understand the filament self-organisation. While the task ahead is immense, we hope that this paper answers some questions while introducing new ones, the most intriguing being the observed planar configuration of 3 filaments.

5. Conclusions

Depending on the experimental conditions, the MW plasma torch operated in atmospheric pressure argon can produce one or more linear plasma filament(s). It was found that MW power is the main parameter that affects the number and stability of the filaments. Stable configurations with up to three filaments were observed. The case of three filaments was peculiar as their preferred spatial pattern was planar and not triangular.

Several observations (axial profiles of electron density and light emission, radial profile of light emission, etc) strongly

support the hypothesis that a SW is exciting the plasma filament while propagating along the surface.

It was found that the transition to a higher number of filaments by splitting may be governed by reaching a critical diameter of the parent filament. Consequently, the skin effect is believed to be responsible.

Based on the rotational temperature obtained from OES and Schlieren imaging, the gas temperature profile is substantially wider than that of luminous plasma.

Imaging and OES revealed the existence of a spatially separated plasma shell around each filament with distinctive spectral differences from the main filament(s).

Acknowledgments

This work was supported by The Czech Science Foundation under Project 18-08520S and in part by Project LM2018097 funded by the Ministry of Education, Youth and Sports of the Czech Republic.

Data availability statement

The data that support the findings of this study are available upon reasonable request from the authors.

ORCID iDs

Miroslav Snirer https://orcid.org/0000-0003-0534-5262
Jozef Toman https://orcid.org/0000-0002-8391-8073
Vít Kudrle https://orcid.org/0000-0002-7669-1691
Ondřej Jašek https://orcid.org/0000-0002-1416-794X

References

[1] Samukawa S *et al* 2012 *J. Phys. D: Appl. Phys.* **45** 253001
[2] Tendero C, Tixier C, Tristant P, Desmaison J and Leprince P 2006 *Spectrochim. Acta* B **61** 2–30
[3] Weltmann K D, Kindel E, von Woedtke T, Hähnel M, Stieber M and Brandenburg R 2010 *Pure Appl. Chem.* **82** 1223–37
[4] Schlüter H and Shivarova A 2007 *Phys. Rep.* **443** 121–255
[5] Atanassov V and Mateev E 2007 *J. Phys.: Conf. Ser.* **63** 012025
[6] Lishev S, Marinova L, Schlüter H and Shivarova A 2002 *Vacuum* **69** 153–8
[7] Medvedev A and Pinaev P 2021 *AIP Conf. Proc.* **2351** 030081
[8] Ridenti M A, de Amorim J, Dal Pino A, Guerra V and Petrov G 2018 *Phys. Rev.* E **97** 013201
[9] Bazelyan E M and Raizer Y P 2000 *Lightning Physics and Lightning Protection* (Boca Raton, FL: CRC Press)
[10] Kekez M M, Barrault M R and Craggs J D 1970 *J. Phys. D: Appl. Phys.* **3** 1886
[11] Poritskii P V 2006 *High Temp.* **44** 328–35
[12] Kogelschatz U 2002 *IEEE Trans. Plasma Sci.* **30** 1400–8
[13] Brandenburg R 2017 *Plasma Sources Sci. Technol.* **26** 053001
[14] Schäfer J, Sigeneger F, Šperka J, Rodenburg C and Foest R 2017 *Plasma Phys. Control. Fusion* **60** 014038
[15] Teodorescu M, Bazavan M, Ionita E R and Dinescu G 2015 *Plasma Sources Sci. Technol.* **24** 025033
[16] Van der Mullen J J A M, Van de Sande M J, De Vries N, Broks B, Iordanova E, Gamero A, Torres J and Sola A 2007 *Spectrochim. Acta* B **62** 1135–46
[17] Rincón R, Muñoz J, Sáez M and Calzada M D 2013 *Spectrochim. Acta* B **81** 26–35
[18] Kubečka M, Snirer M, Obrusník A, Kudrle V and Bonaventura Z 2020 *Plasma Sources Sci. Technol.* **29** 075001
[19] Jankowski K J and Reszke E 2011 *Microwave induced Plasma Analytical Spectrometry* (*RSC Analytical Spectroscopy Monographs*) vol 12 (Cambridge: The Royal Society of Chemistry)
[20] Martinez E C, Kabouzi Y, Makasheva K and Moisan M 2004 *Phys. Rev.* E **70** 066405
[21] Massey J T and Cannon S M 1965 *J. Appl. Phys.* **36** 361–72
[22] Kudela J, Odrobina I and Kando M 1998 *Japan J. Appl. Phys.* **37** 4169
[23] Moisan M and Pelletier J 2012 *Physics of Collisional Plasmas: Introduction to High-Frequency Discharges* (Berlin: Springer)
[24] Kabouzi Y, Calzada M D, Moisan M, Tran K C and Trassy C 2002 *J. Appl. Phys.* **91** 1008–19
[25] Kabouzi Y and Moisan M 2005 *IEEE Trans. Plasma Sci.* **33** 292–3
[26] Viegas P, Vialetto L, Wolf A J, Peeters F J J, Groen P W C, Righart T W H, Bongers W A, Van de Sanden M C M and Diomede P 2020 *Plasma Sources Sci. Technol.* **29** 105014
[27] Castaños-Martínez E, Moisan M and Kabouzi Y 2008 *J. Phys. D: Appl. Phys.* **42** 012003
[28] Cardoso R P, Belmonte T, Noël C, Kosior F and Henrion G 2009 *J. Appl. Phys.* **105** 093306
[29] Hnilica J, Kudrle V, Vašina P, Schäfer J and Aubrecht V 2012 *J. Phys. D: Appl. Phys.* **45** 055201
[30] Li P, Chen Z, Mu H, Xu G, Yao C, Sun A, Zhou Y and Zhang G 2018 *J. Appl. Phys.* **123** 123302
[31] Muñoz J, Bravo J A and Calzada M D 2009 *Open Spectrosc. J.* **3**
[32] Iza F and Hopwood J A 2005 *IEEE Trans. Plasma Sci.* **33** 306–7
[33] Allison J, Cullen A L and Závody A 1962 *Nature* **193** 156
[34] Boeuf J P, Chaudhury B and Zhu G Q 2010 *Phys. Rev. Lett.* **104** 015002
[35] Chaudhury B and Boeuf J-P 2010 *IEEE Trans. Plasma Sci.* **38** 2281–8
[36] Wolf A J, Righart T W H, Peeters F J J, Groen P W C, Van De Sanden M C M and Bongers W A 2019 *Plasma Sources Sci. Technol.* **28** 115022
[37] Maximov A V and Schlüter H 2002 *Phys. Scr.* **65** 263
[38] Skovoroda A A and Zvonkov A V 2001 *J. Exp. Theor. Phys.* **92** 78–85
[39] Kong M G, Kroesen G, Morfill G, Nosenko T, Shimizu T, Van Dijk J and Zimmermann J L 2009 *New J. Phys.* **11** 115012
[40] Potočňáková L, Hnilica J and Kudrle V 2013 *Int. J. Adhes. Adhes.* **45** 125–31
[41] Wattieaux G, Yousfi M and Merbahi N 2013 *Spectrochim. Acta* B **89** 66–76
[42] Henriques J, Bundaleska N, Tatarova E, Dias F M and Ferreira C M 2011 *Int. J. Hydrogen Energy* **36** 345–54
[43] Snoeckx R and Bogaerts A 2017 *Chem. Soc. Rev.* **46** 5805–63
[44] Bogaerts A and Centi G 2020 *Front. Energy Res.* **8** 111
[45] David B, Pizúrová N, Synek P, Kudrle V, Jašek O and Schneeweiss O 2014 *Mater. Lett.* **116** 370–3
[46] Šnírer M, Zelina P and Kudrle V 2014 *IEEE Trans. Plasma Sci.* **42** 2778–9
[47] Zajíčková L, Synek P, Jašek O, Eliáš M, David B, Buršík J, Pizúrová N, Hanzlíková R and Lazar L 2009 *Appl. Surf. Sci.* **255** 5421–4
[48] Prasek J, Drbohlavova J, Chomoucka J, Hubalek J, Jasek O, Adam V and Kizek R 2011 *J. Mater. Chem.* **21** 15872–84

[49] Toman J, Jašek O, Snirer M, Kudrle V and Jurmanová J 2019 *J. Phys. D: Appl. Phys.* **52** 265205
[50] Jašek O *et al* 2021 *J. Phys. D: Appl. Phys.* **54** 165201
[51] Lu X, Reuter S, Laroussi M and Liu D 2019 *Nonequilibrium Atmospheric Pressure Plasma Jets: Fundamentals, Diagnostics, and Medical Applications* (Boca Raton, FL: CRC Press)
[52] Bruggeman P and Brandenburg R 2013 *J. Phys. D: Appl. Phys.* **46** 464001
[53] Xian Y, Yue Y, Liu D, Yang Y, Lu X and Pan Y 2014 *Plasma Process. Polym.* **11** 1169–74
[54] Schäfer J, Foest R, Ohl A and Weltmann K-D 2009 *Plasma Phys. Control. Fusion* **51** 124045
[55] Van der Mullen J, Atanasova M, Obrusník A and Zajíčková L 2020 *J. Anal. At. Spectrom.* **35** 2064–74
[56] Moisan M, Sauve G, Zakrzewski Z and Hubert J 1994 *Plasma Sources Sci. Technol.* **3** 584
[57] Ricard A, St-Onge L, Malvos H, Gicquel A, Hubert J and Moisan M 1995 *J. Phys. III France* **5** 1269–85
[58] Moisan M, Zakrzewski Z and Rostaing J C 2001 *Plasma Sources Sci. Technol.* **10** 387
[59] Snirer M, Kudrle V, Toman J, Jašek O and Jurmanová J 2021 *Plasma Plasma Sources Sci. Technol.* **30** 065020
[60] Toman J *et al* 2021 *Plasma Process. Polym.* **18** e2100008
[61] Hendriks C L, Van Vliet L, Rieger B, van Kempen G and van Ginkel M 1999 *Quantitative Imaging Group* (Delft, The Netherlands: Faculty of Applied Sciences, Delft University of Technology)
[62] Hickstein D D, Gibson S T, Yurchak R, Das D D and Ryazanov M 2019 *Rev. Sci. Instrum.* **90** 065115
[63] Álvarez R, Quintero M C and Rodero A 2004 *Spectrochim. Acta* B **59** 709–21
[64] Moisan M and Nowakowska H 2018 *Plasma Sources Sci. Technol.* **27** 073001
[65] Moisan M and Zakrzewski Z 1991 *J. Phys. D: Appl. Phys.* **24** 1025
[66] Nowakowska H, Zakrzewski Z and Moisan M 2001 *J. Phys. D: Appl. Phys.* **34** 1474
[67] Jonkers J, Selen L J M, van der Mullen J A M, Timmermans E A H and Schram D C 1997 *Plasma Sources Sci. Technol.* **6** 533
[68] Faltýnek J, Kudrle V, Šnírer M, Toman J and Jašek O 2021 *Plasma Sources Sci. Technol.* **30** 015001
[69] Synek P, Obrusník A, Hübner S, Nijdam S and Zajíčková L 2015 *Plasma Plasma Sources Sci. Technol.* **24** 025030
[70] Green K M, Borras M C, Woskov P P, Flores G J, Hadidi K and Thomas P 2001 *IEEE Trans. Plasma Sci.* **29** 399–406
[71] Zajíčková L, Eliáš M, Jašek O, Kudrle V, Frgala Z, Matějková J, Buršík J and Kadlečíková M 2005 *Plasma Phys. Control. Fusion* **47** B655
[72] Maximov A V and Schlüter H 1999 *Phys. Scr.* **60** 556
[73] Lishev S, Shivarova A and Tarnev K 2008 *J. Appl. Phys.* **103** 013304
[74] Álvarez R and Alves L L 2007 *J. Appl. Phys.* **101** 103303
[75] Bogaczyk M, Wild R, Stollenwerk L and Wagner H-E 2012 *J. Phys. D: Appl. Phys.* **45** 465202
[76] Zeldovich Y B 2014 *Selected Works of Yakov Borisovich Zeldovich* (*Chemical Physics and Hydrodynamics* vol 1) (Princeton, NJ: Princeton University Press)
[77] Burnette D, Montello A, Adamovich I V and Lempert W R 2014 *Plasma Sources Sci. Technol.* **23** 045007
[78] Gaens W V, Bruggeman P J and Bogaerts A 2014 *New J. Phys.* **16** 063054
[79] Iseni S, Zhang S, Van Gessel A F H, Hofmann S, Van Ham B T J, Reuter S, Weltmann K-D and Bruggeman P J 2014 *New J. Phys.* **16** 123011
[80] Sarani A, Nikiforov A Y and Leys C 2010 *Phys. Plasmas* **17** 063504
[81] Voráč J, Synek P, Potočňáková L, Hnilica J and Kudrle V 2017 *Plasma Sources Sci. Technol.* **26** 025010
[82] Voráč J, Synek P, Procházka V and Hoder T 2017 *J. Phys. D: Appl. Phys.* **50** 294002
[83] Bruggeman P J, Sadeghi N, Schram D C and Linss V 2014 *Plasma Sources Sci. Technol.* **23** 023001
[84] Muñoz J, Margot J and Calzada M D 2010 *J. Appl. Phys.* **107** 083304
[85] Christova M, Castaños-Martinez E, Calzada M D, Kabouzi Y, Luque J M and Moisan M 2004 *Appl. Spectrosc.* **58** 1032–7
[86] Moon S Y and Choe W 2003 *Spectrochim. Acta* B **58** 249–57
[87] Rodero A, García M C, Quintero M C, Sola A and Gamero A 1996 *J. Phys. D: Appl. Phys.* **29** 681